scientific reports

Check for updates

OPEN

Directional charge delocalization dynamics in semiconducting 2H-MoS_2 and metallic 1T-Li_xMoS_2

Robert Haverkamp[1,2]✉, Nomi L. A. N. Sorgenfrei[1], Erika Giangrisostomi[1], Stefan Neppl[1], Danilo Kühn[1] & Alexander Föhlisch[1,2]

The layered dichalcogenide MoS_2 is relevant for electrochemical Li adsorption/intercalation, in the course of which the material undergoes a concomitant structural phase transition from semiconducting 2H-MoS_2 to metallic 1T-Li_xMoS_2. With the core hole clock approach at the S L_1 X-ray absorption edge we quantify the ultrafast directional charge transfer of excited S3p electrons in-plane (∥) and out-of-plane (⊥) for 2H-MoS_2 as $\tau_{2H,\parallel} = 0.38 \pm 0.08$ fs and $\tau_{2H,\perp} = 0.33 \pm 0.06$ fs and for 1T-Li_xMoS_2 as $\tau_{1T,\parallel} = 0.32 \pm 0.12$ fs and $\tau_{1T,\perp} = 0.09 \pm 0.07$ fs. The isotropic charge delocalization of S3p electrons in the semiconducting 2H phase within the S-Mo-S sheets is assigned to the specific symmetry of the Mo-S bonding arrangement. Formation of 1T-Li_xMoS_2 by lithiation accelerates the in-plane charge transfer by a factor of ∼ 1.2 due to electron injection to the Mo-S covalent bonds and concomitant structural repositioning of S atoms within the S-Mo-S sheets. For excitation into out-of-plane orbitals, an accelerated charge transfer by a factor of ∼ 3.7 upon lithiation occurs due to S-Li coupling.

Layered quasi-2D transition metal dichalcogenides (TMDs) are highly anisotropic crystals[1–3] that are attractive for numerous fields of applications due to their unique inherent properties. Whereas the intralayer interaction is characterized by strong covalent bonding in these materials, the interlayer coupling by weak van der Waals (vdW) forces make layered TMDs amenable to intercalation of foreign atoms and molecules. In particular, molybdenum disulfide (MoS_2) based devices span the fields of photovoltaics[4], hydrogen production[5,6], electronics[7], optoelectronics[8] and even extend to the implementation of MoS_2 in future memresistive circuits and related applications[9,10]. Extraordinary capabilities have been demonstrated for MoS_2 based electrodes in rechargeable, high capacity lithium ion batteries (LIBs)[11] as well as high energy and power density supercapacitors[12] based on the efficient Li^+ intercalation.

MoS_2 possesses a repeated structure of S-Mo-S sheets occurring in distinct symmetries. The two most important polytypes are the naturally occurring 2H and the 1T allotropes[13,14]. While 2H-MoS_2 is a semiconductor with a layer dependent bandgap that increases from about 1.2 eV in the bulk up to about 1.9 eV for a monolayer[15,16], 1T-MoS_2 is metallic with the Fermi level within the Mo d-band[17]. On a structural level, the transition from the hexagonal 2H phase with vertically aligned S atoms to the trigonal 1T structure corresponds to a collective shear displacement of S atoms equivalent to a 60° rotation of one plane of S atoms[17].

Both, experimental and computational studies show that the 2H-semiconductor to 1T-metal phase transition can be induced by electron injection into the 2H-MoS_2 crystal. Upon this charge doping, partial population of the Mo4d orbitals by an extra electron destabilizes the 2H crystal structure and leads to the transition into the 1T phase[14,18,19]. Experimentally this charge injection has been realized by electron microscopy[20,21], laser excitation of deposited plasmonic nanoparticles[22] and by alkali metal intercalation[14,23], where Li atoms are the most efficient and commonly applied dopants.

Li with its $1s^2 2s^1$ electronic configuration can inject a 2s electron into the conduction band minimum of the 2H-MoS_2 crystal as the Li^+ cation is adsorbed and/or intercalated, leading to the formation of 1T-Li_xMoS_2[14]. It has been demonstrated that, once MoS_2 based electrodes are loaded with Li atoms, 1T-Li_xMoS_2 is not reversed back into 2H-MoS_2 anymore, but remains in the 1T phase. Thus loading cycles are not limited by structural fatigue from repeated volumetric changes between the 2H and 1T structure[12].

[1]Methods and Instrumentation for Synchrotron Radiation Research PS-ISRR, Helmholtz-Zentrum Berlin für Materialien und Energie GmbH, Albert-Einstein-Straße 15, 12489 Berlin, Germany. [2]Institut für Physik und Astronomie, Universität Potsdam, Karl-Liebknecht-Straße 24/25, 14476 Potsdam, Germany. ✉email: Robert.Haverkamp@Helmholtz-Berlin.de

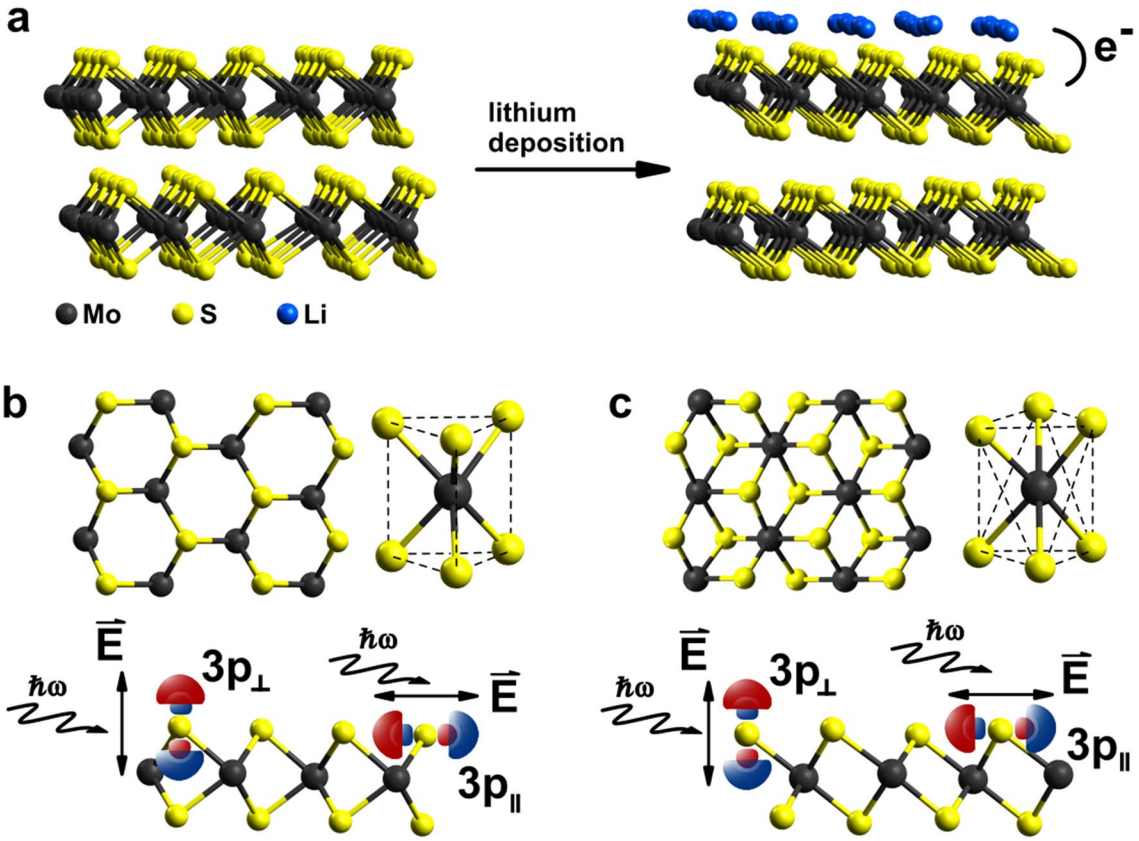

Figure 1. Structure of the semiconducting 2H and the metallic 1T phase of MoS_2 and the directional excitation of an electron into unoccupied S3p states following absorption of linearly polarized X-rays at the S L_1-edge in the CHC experiment. (**a**) Lithium deposition onto 2H-MoS_2 leads to concomitant intercalation/adsorption of Li^+ cations and electron injection, causing the phase transition and formation of 1T-Li_xMoS_2. (**b**, **c**) Crystallographic structures in top- and side-views of a monolayer of the 2H and the 1T phase. CHC spectroscopy prepares selectively in-plane (∥) and out-of-plane (⊥) S3p excited states. Black, yellow and blue spheres represent Mo, S and Li atoms, respectively. The crystallographic structure was build using Avogadro software version 1.2.0[32] and edited with Inkscape software version 0.92.3 (www.inkscape.org).

An essential property that influences the performance of e.g. LIBs and supercapacitors is the electron mobility. In this context, our work provides access to the in- and out-of-plane electron transfer dynamics in 2H-MoS_2 and 1T-Li_xMoS_2, relevant for electrochemical Li loading of MoS_2 based electrode materials, on the atomic level. Here the orbital specificity and sub-fs capabilities of the core-hole clock (CHC) method[24,25] are essential since previously applied laser-based pump-probe investigations on MoS_2 and related heterostructures[26,27] are limited on the few tens of fs timescale and lack of ability to provide directional selectivity. The CHC method has already been successfully applied to determine charge transfer dynamics in TaS_2[28] and different MoS_2 based heterojunctions[29–31], demonstrating its capability for measuring the directional charge transfer in layered TMDs. The basic principle of the CHC spectroscopy is elucidated in the methods section.

Results and discussion

Figure 1 summarizes the essence of the structural properties of 2H-MoS_2 and 1T-Li_xMoS_2 as well as the preparation of 1T-Li_xMoS_2 through electron injection following Li adsorption and/or intercalation. Finally it also shows how the CHC method allows to detect in-plane and out-of-plane charge transfer times of an electron excited into S3p in-plane and out-of-plane orbital states, respectively. Figure 1a depicts schematically how *in situ* Li deposition directly onto the clean 2H-MoS_2 surface leads to the 1T phase, following the ultra-high vacuum (UHV) compatible preparation described by Papageorgopoulos et al[23], with further details given in the methods section. This UHV compatible approach has shown to lead to the same 1T-Li_xMoS_2 phase equivalently as do methods involving alkali solution[5,12] or electrochemical preparations[13,14]. It has been shown that the 1T phase, prepared by lithiation of MoS_2, stabilizes locally though lattice distortions by forming the so-called 1T' structure which results in the coexistence of the 1T and the distorted 1T' crystallographic structure within the MoS_2 lattice[33]. The differentiation between the 1T/1T' and 2H phase has been verified independently by techniques like Raman-[4–6,22,34], photoluminescence-[22,35], X-ray photoelectron spectroscopy (XPS)[4,6,35], high-resolution electron microscopy[4,21], nanomechanics[36] and can also be accomplished by valence band photo emission[37]. While laser based optical methods like Raman spectroscopy as well as electron microscopy are suitable techniques to study the crystallographic phase and therefore allow the unambiguous determination of the 1T and 1T' structure in

MoS_2, it has been shown that both methods depending on the laser power[38], respectively the electron dose[21], influence the crystallographic phase. We confirmed the successful phase transition upon lithiation by *in situ* XPS of the valence band as well as the established S2p and Mo3d core level binding energies[23]. XPS offers the advantage that it allows to detect the 2H to 1T/1T' phase transition as well as the phase ratio by means of the S2p and Mo3d core level binding energies while valence band measurements clearly reveal the semiconductor to metal transition. However, it does not allow to distinguish the 1T and 1T' structure. For that reason, hereinafter 1T will implicate both the undistorted and the distorted crystallographic phase. In our experiments, we achieved for our lithiated MoS_2 crystal a 1T phase concentration of 86 ± 5 % in the detection volume (quantitative fitting routine in the supplementary information).

In Fig. 1b,c we show the detailed structural properties within each S-Mo-S sheet for MoS_2 in the 2H (Fig. 1b) and 1T (Fig. 1c) phase. We also illustrated a representation of the directional selectivity based on the resonant excitation of an S2s core electron into the unoccupied $S3p_{\parallel}$ or $S3p_{\perp}$ conduction band states following the absorption of linearly polarized X-rays with the electric field vector pointing parallel or perpendicular to the MoS_2 sheet orientation, respectively[24,25]. We note that even though the 2H and 1T phase differ in the local microscopic structure, the S2s → S3p dipole transition generates equivalent in-plane $S3p_{\parallel}$ and out-of-plane $S3p_{\perp}$ orbital populations in both phases.

Figure 2 shows polarization dependent S $L_1L_{2,3}M_{1,2,3}$ Coster-Kronig (CK) autoionization spectra, for 2H-MoS_2 (Fig. 2a,c) and 1T-Li_xMoS_2 (Fig. 2b,d) as a function of incident photon energy. The photon energy has been tuned for in-plane and out-of-plane polarization across the S L_1 absorption edge from 224 eV to 236 eV. The autoionization electron spectra from the S $L_1L_{2,3}M_{1,2,3}$ CK decay are monitored in the kinetic energy range from 30 eV to 65 eV. In order to quantitatively evaluate the CK autoionization decay channels, all spectral features corresponding to direct S2p photoionization, shake-up and the secondary electron background have been subtracted according to a previously reported procedure[24,25]. A detailed description of the data analysis is given in the supporting information. Depending on the final state reached in the CK decay and based on their characteristic dispersive behaviour with the incoming X-ray photon energy, competing decay channels can be distinguished. For the Raman-channels $S2p^{-1}3s^{-1}3p^1$ (l) and $S2p^{-1}3p^{-1}3p^1$ (L) at constant binding energy the resonantly excited electron remains localized at the atomic site within the core hole lifetime. In contrast, the Auger-channels $S2p^{-1}3s^{-1}deloc.^1$ (d) and $S2p^{-1}3p^{-1}deloc.^1$ (D) appear at constant kinetic energy, which is the signature of S3p electron delocalization within the conduction band during the timescale of the S2s core hole decay, i.e. charge transfer occurred. At the resonance maximum of the S L_1-edge at a photon energy $h\nu_{res} = 228.5 \pm 0.1$ eV, the Raman-channels branch into charge transfer Auger-channels for both 2H-MoS_2 and 1T-Li_xMoS_2. For 2H-MoS_2 the d- and D-channel are found at a kinetic energy of 40.4 eV (d) and 50.8 eV (D) while for 1T-Li_xMoS_2 they are found at 38 eV (d) and 50.4 eV (D), respectively.

The quantitative analysis of the autoionization branching ratios and the related charge transfer times is based on the l- and d-channels, as these are spectrally pure autoionization final states[24]. As a function of incident photon energy, the intensities of the l- and d-channels are plotted in the lower panel below each resonant photoemission spectrum in Fig. 2. At and above resonance, both the localized Raman-channel (l) and delocalized Auger-channel (d) coexist with intensities I_{Raman} and I_{Auger}. Below resonance only the Raman-channel is observable. With the CHC rate model $\tau_{CT} = I_{Raman}/I_{Auger} \cdot \tau_{S2s}$ using the natural S2s core hole lifetime $\tau_{S2s} = 0.51$ fs[39], the timescale for charge delocalization can be determined in a range spanning $0.051 \text{ fs} < \tau_{CT} < 5.1 \text{ fs}$[24]. Following this procedure, a quantitative evaluation of the in- and out-of-plane charge transfer times τ_{CT} has been performed for 2H-MoS_2 and 1T-Li_xMoS_2.

Figure 3 summarizes the extracted charge transfer times of $S3p_{\parallel}$ and $S3p_{\perp}$ excited states as a function of the X-ray photon energy for 2H-MoS_2 (Fig. 3a) and 1T-Li_xMoS_2 (Fig. 3b) based on the spectral intensities from Fig. 2. A slight variation of charge transfer above threshold excitation can be seen. The evaluation of the charge transfer times will be restricted to the photon energy range from 229.5 eV to 230.5 eV just above the S2s → S3p X-ray absorption resonance maximum (shaded in Fig. 3).

Semiconducting 2H-MoS_2 has S3p charge transfer times of $\tau_{2H,\parallel} = 0.38 \pm 0.08$ fs in-plane and $\tau_{2H,\perp} = 0.33 \pm 0.06$ fs out-of-plane. Metallic 1T-Li_xMoS_2 has S3p charge transfer times of $\tau_{1T,\parallel} = 0.32 \pm 0.12$ fs in-plane and $\tau_{1T,\perp} = 0.09 \pm 0.07$ fs out-of-plane. By and large, the charge transfer in metallic 1T-Li_xMoS_2 is for all directions faster in comparison to the semiconducting situation of 2H-MoS_2.

We start our discussion with the charge transfer dynamics in 2H-MoS_2. It is apparent from Fig. 3a that there is no significant difference between the in-plane and out-of-plane charge transfer times within the error margin. At first sight, this isotropic charge transfer seems puzzling, regarding the quasi-2D character displayed macroscopically by layered 2H-MoS_2. However, this result is explained, if we consider the local hexagonal arrangement of the S atoms around the Mo atoms within each S-Mo-S sheet as depicted in Fig. 1b: both the S2s → $S3p_{\parallel}$ and S2s → $S3p_{\perp}$ excitation populates orbitals, which have similar projections onto the direction of the angled covalent Mo-S bonds. Consequently equivalent $S3p_{\parallel}$ and $S3p_{\perp}$ charge transfer time constants are measured. This quasi-isotropic charge transfer in 2H-MoS_2 has been brought to attention previously by hard X-ray S K-edge CHC studies derived from systematically varied layer structures of MoS_2[30]. It has been proposed that the weak vdW interaction between adjacent MoS_2 layers is negligible[30], and that intralayer electronic coupling must be the dominant delocalization pathway, which is in agreement with our microscopic explanation based on linear superposition of angled Mo-S bonds and the resulting isotropic $S3p_{\parallel}$ and $S3p_{\perp}$ charge transfer.

In contrast to the isotropic charge transfer in semiconducting 2H-MoS_2, highly anisotropic and faster charge transfer characteristics are found for metallic 1T-Li_xMoS_2. Charge transfer from in-plane $S3p_{\parallel}$ orbitals within 1T-Li_xMoS_2 accelerates by a factor of ∼ 1.2 compared to 2H-MoS_2. As depicted in Fig. 1, electron injection upon lithiation into the Mo-S bonds is linked to a structural shift equivalent to a 60° rotation of one full S atom plane. Thus, this change of occupancy in the Mo-S covalent bonds with concomitant structural changes is sensitively reflected by the in-plane $S3p_{\parallel}$ charge transfer acceleration.

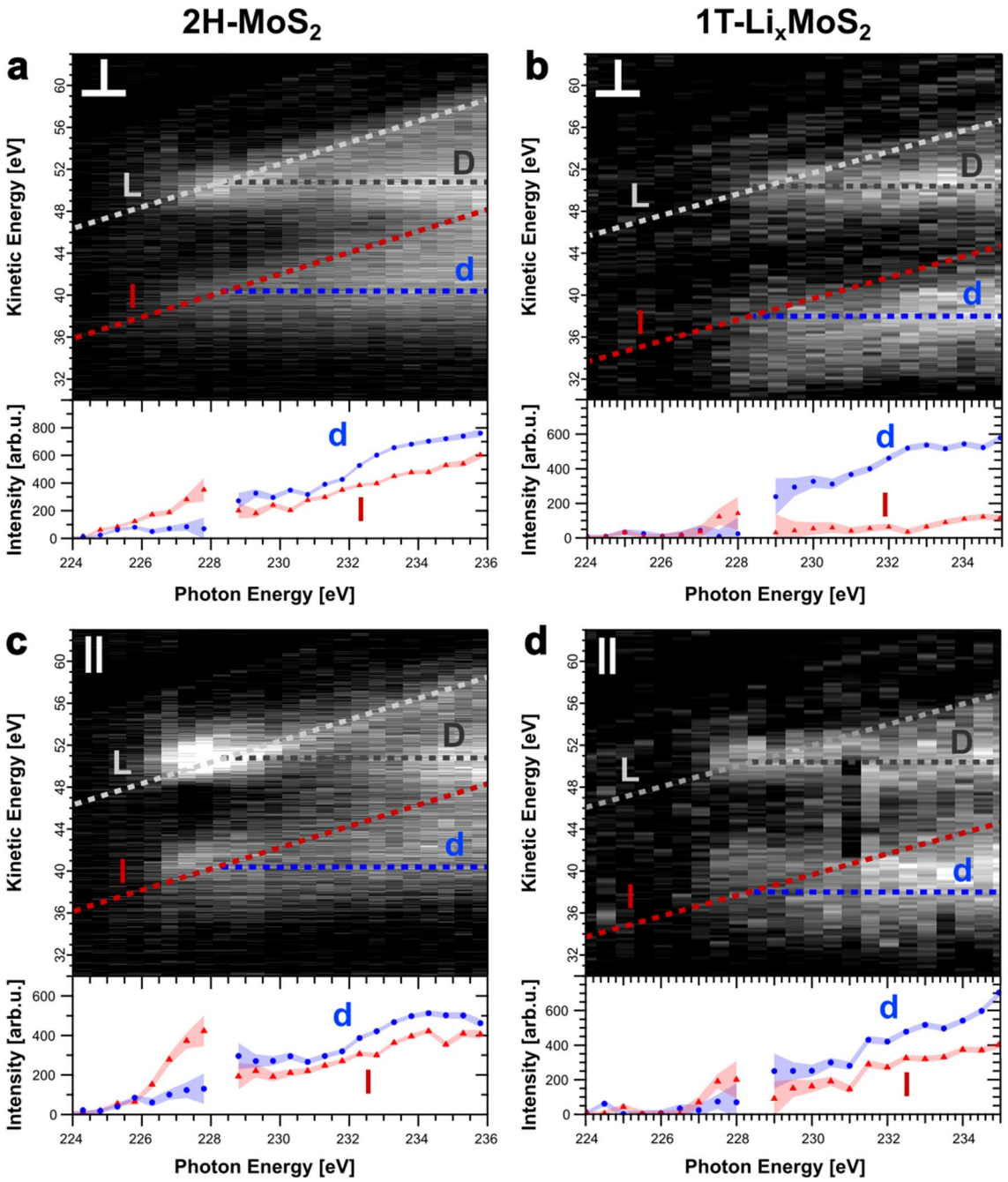

Figure 2. Polarization dependent S $L_1L_{2,3}M_{1,2,3}$ CK autoionization spectra as a function of incident X-ray energy for 2H-MoS_2 (**a**,**c**) and 1T-Li_xMoS_2 (**b**,**d**). The Raman-channels l ($S2p^{-1}3s^{-1}3p^1$) and L ($S2p^{-1}3p^{-1}3p^1$) as well as the Auger-channels d ($S2p^{-1}3s^{-1}$deloc.^{1}) and D ($S2p^{-1}3p^{-1}$deloc.^{1}) are indicated. The symbols ∥ and ⊥ denote the selective preparation of in- and out-of-plane S3p excited states. The region of the direct S2p photoionization lines has been subtracted. Below each autoionization spectrum, the spectral intensities of the l- and d-channels are plotted as a function of the photon energy. Error bars represent the uncertainty of each individual fit.

The out-of-plane charge transfer in 1T-Li_xMoS_2 takes place on a significantly shorter timescale, corresponding to an acceleration by a factor of $\sim$ 3.7 compared to 2H-MoS_2. The value of $\tau_{1T,\perp}$ should be considered as an upper limit for the out-of-plane charge transfer time for the following reasons: our experimental geometry of 15° grazing incidence adds a geometrical fraction of the slower in-plane charge transfer time to the faster out-of-plane component and our 1T-Li_xMoS_2 crystal preparation with an average 1T phase concentration of 86 ± 5 % in the detection volume admixes some slower components from the coexisting 2H phase.

The key question is whether the significant acceleration of the out-of-plane charge transfer can be linked to the electronically and structurally changed properties of the semiconducting 2H-MoS_2 and metallic 1T-Li_xMoS_2. As the distance between the vdW coupled S-Mo-S sheets increases in response to the lithiation and phase transition,

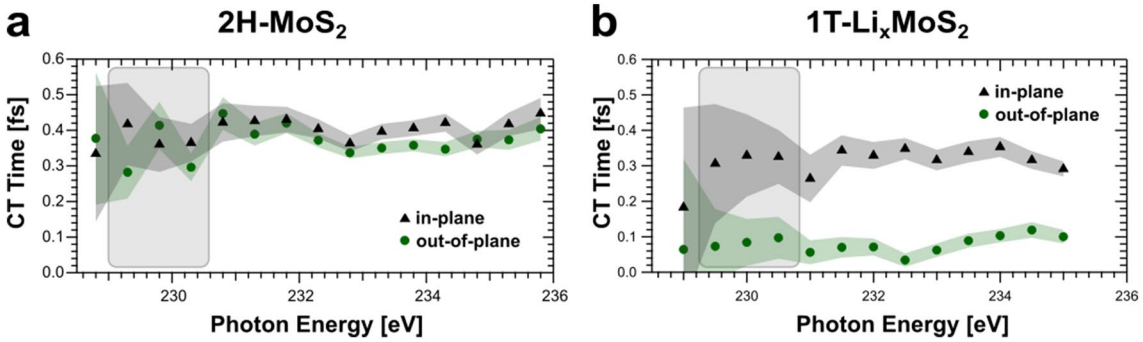

Figure 3. In-plane $\tau_{\parallel}$ (black triangles) and out-of-plane $\tau_{\perp}$ (green circles) charge transfer times of S3p excited states in 2H-MoS_2 (**a**) and 1T-Li_xMoS_2 (**b**) from CHC analysis of Auger- (d) and Raman-channels (l) and the natural S2s core hole lifetime. Resonant excitation into the conduction band minimum occurs for incident photon energies 229.5 eV to 230.5 eV just above the S2s → S3p X-ray absorption resonance maximum. Error bars (shaded) for each photon energy, orientation and sample result from error propagation through the CHC analysis from the fitted intensities (Fig. 2) of each underlying autoionization spectrum.

no additional overlap between S orbitals in neighboring S-Mo-S sheets can be the root cause[6,12]. In addition the electron injection upon lithiation and the concomitant 60° rotation of one full S atom plane changes the composition of the Mo-S angled bond for the out-of-plane and the in-plane projection in a similar fashion. Thus, the electron sharing between adsorbed/intercalated Li atoms with the S atoms of the S-Mo-S sheets seems to be the dominant process driving the accelerated $S3p_{\perp}$ charge transfer in 1T-Li_xMoS_2. This explanation is substantiated by a comparison with adsorbed P3HT molecules on MoS_2 in the form of a P3HT/MoS_2/SiO_2 heterojunction[29]. The referred study showed that deposition of the conducting P3HT polymer molecules onto the MoS_2 monolayer leads to an n-doping (electron injection from the molecular donor into the MoS_2 film) accompanied by accelerated out-of-plane charge transfer of $\sim$ 50 %, whereas the in-plane charge transfer is unaffected. In this system, overlap between the surface adsorbed P3HT frontier orbitals and S3p states can be the only cause for an efficient out-of-plane electron delocalization pathway, in particular since the other side of the heterojunction has insulating SiO_2 as a substrate. In analogy to the case of the P3HT/MoS_2/SiO_2 heterojunction, we conclude that the acceleration of $\tau_{1T,\perp}$ by a factor of $\sim$ 3.7 compared to $\tau_{2H,\perp}$ in bulk lithiated, metallic 1T-Li_xMoS_2 should also reflect the opening of an additional electron delocalization pathway due to the coupling of the S atoms of the S-Mo-S sheet to the adsorbed/intercalated Li.

With respect to the implementation of MoS_2 in energy storage devices like LIBs and supercapacitors, the results demonstrate that the quasi 2D layered structure, which enables efficient Li intercalation, does not restrict the electron mobility within the layer. In response to the Li intercalation reaction, the charge delocalization times reveal that the charge mobility is increased in both the in- and out-of-plane direction, facilitating charge extraction/insertion independent of the relative electrode orientation to the MoS_2 layers. Further, the results indicate that deposition/intercalation of atoms or molecules has the potential to greatly alter the out-of-plane charge transport properties of MoS_2. For instance, the catalytic performance of MoS_2 for hydrogen production has been shown to be hindered for catalytic active sites being separated from the conductive substrate by parallel oriented MoS_2 layers[40]. On this basis, deposition/intercalation could be used to modify out-of-plane charge mobility in MoS_2 to improve the properties of MoS_2 as a material for applications based on the out-of-plane charge mobility or where functionality is hindered by the interlayer potential barrier.

Methods

Core hole clock method. The principle of the CHC method is based on the resonant excitation of a core electron to an unoccupied state while the finite lifetime of the created core hole serves as an internal reference clock for the decay processes following the initial excitation in the studied system. Following the resonant excitation, competing decay channels of the autoionization process with different dispersive behavior can be observed. A linear dispersion between the X-ray energy and the kinetic energy of the electron is observed for resonantly excited electrons remaining localized within the core hole lifetime (Raman-channel). If the resonantly excited electron is delocalized within the conduction band during the decay process, i.e. charge transfer occurred, the kinetic energy of the ejected electron is independent of the exciting X-ray energy (Auger-channel). Scanning the X-ray energy across the resonance maximum, allows to unambiguously distinguish the different decay channels. The intensity ratio of the competing channels and the respective natural lifetime of the core-excited state are then used to calculate the charge transfer times of the studied system.

XPS measurements. All experimental data presented in this work have been acquired, at the "FEMTOSPEX Molecules and Surfaces" endstation[41], installed at the BESSY II soft X-ray UE56/1 PGM beamline during the single bunch operation mode. The beamline provides adjustable X-ray polarizations (linear vertical and horizontal as well as circular) with a focus spot size on the sample of approximately 200 x 200 μm^2. Absolute energy calibration was obtained by an Argon gas cell installed in the beamline. The data have been collected under ambient temperature and a base pressure in the measurement chamber of $2 \cdot 10^{-10}$ mbar. The presented data have been measured under a grazing X-ray incidence angle of 15°. A VG Scienta-Omicron angle-resolved time

of flight (ARTOF) electron spectrometer with a 60° acceptance angle lens system was used[42]. Further, preliminary measurements have been conducted at the LowDosePES endstation at the BESSY II PM4 dipole beamline.

Sample preparation. Commercial 2H-MoS_2 crystals produced by 2D Semiconductors were cleaved by mechanical exfoliation under UHV conditions at a pressure of $< 10^{-9}$ mbar to ensure a pristine surface and were further annealed for 30 minutes at 460°C. The sample quality was verified by survey XPS spectra, showing no evidence of elements other than Mo and S.

A SAES Getters Li disperser was mounted at the chamber to achieve a controlled Li deposition directly onto the clean 2H-MoS_2 crystal surface. The total Li deposition time amounts to 80 minutes with a background pressure of $\sim 1 \cdot 10^{-8}$ mbar to successfully promote the transition to metallic 1T-Li_xMoS_2.

Received: 13 January 2021; Accepted: 11 March 2021
Published online: 25 March 2021

References

1. Gehlmann, M. *et al.* Quasi 2D electronic states with high spin-polarization in centrosymmetric MoS_2 bulk crystals. *Sci. Rep.* **6**, 26197. https://doi.org/10.1038/srep26197 (2016).
2. Riley, J. M. *et al.* Direct observation of spin-polarized bulk bands in an inversion-symmetric semiconductor. *Nat. Phys.* **10**, 835–839. https://doi.org/10.1038/nphys3105 (2014).
3. Tongay, S. *et al.* Monolayer behaviour in bulk ReS_2 due to electronic and vibrational decoupling. *Nat. Commun.* **5**, 3252. https://doi.org/10.1038/ncomms4252 (2014).
4. Wei, W., Sun, K. & Hu, Y. H. An efficient counter electrode material for dye-sensitized solar cells - flower-structured 1T metallic phase MoS_2. *J. Mater. Chem. A* **4**, 12398–12401. https://doi.org/10.1039/c6ta04743b (2016).
5. Pi, Y. *et al.* 1T-phase MoS_2 nanosheets on TiO_2 nanorod arrays: 3D photoanode with extraordinary catalytic performance. *ACS Sustain. Chem. Eng.* **5**, 5175–5182. https://doi.org/10.1021/acssuschemeng.7b00518 (2017).
6. Geng, X. *et al.* Pure and stable metallic phase molybdenum disulfide nanosheets for hydrogen evolution reaction. *Nat. Commun.* **7**, 10672. https://doi.org/10.1038/ncomms10672 (2016).
7. Radisavljevic, B., Radenovic, A., Brivio, J., Giacometti, V. & Kis, A. Single-layer MoS_2 transistors. *Nat. Nanotechnol.* **6**, 147–150. https://doi.org/10.1038/nnano.2010.279 (2011).
8. Lee, H. S. *et al.* MoS_2 nanosheet phototransistors with thickness-modulated optical energy gap. *Nano Lett.* **12**, 3695–3700. https://doi.org/10.1021/nl301485q (2012).
9. Sangwan, V. K. *et al.* Gate-tunable memristive phenomena mediated by grain boundaries in single-layer MoS_2. *Nat. Nanotechnol.* **10**, 403–406. https://doi.org/10.1038/nnano.2015.56 (2015).
10. Zhu, X., Li, D., Liang, X. & Lu, W. D. Ionic modulation and ionic coupling effects in MoS_2 devices for neuromorphic computing. *Nat. Mater.* **18**, 141–148. https://doi.org/10.1038/s41563-018-0248-5 (2019).
11. Liu, Y., Zhao, Y., Jiao, L. & Chen, J. A graphene-like MoS_2/graphene nanocomposite as a highperformance anode for lithium ion batteries. *J. Mater. Chem. A* **2**, 13109–13115. https://doi.org/10.1039/c4ta01644k (2014).
12. Acerce, M., Voiry, D. & Chhowalla, M. Metallic 1T phase MoS_2 nanosheets as supercapacitor electrode materials. *Nat. Nanotechnol.* **10**, 313–318. https://doi.org/10.1038/nnano.2015.40 (2015).
13. Chhowalla, M. *et al.* The chemistry of two-dimensional layered transition metal dichalcogenide nanosheets. *Nat. Chem.* **5**, 263–275. https://doi.org/10.1038/nchem.1589 (2013).
14. Py, M. A. & Haering, R. R. Structural destabilization induced by lithium intercalation in MoS_2 and related compounds. *Can. J. Phys.* **61**, 76–84. https://doi.org/10.1139/p83-013 (1983).
15. Mak, K. F., Lee, C., Hone, J., Shan, J. & Heinz, T. F. Atomically thin MoS_2: a new direct-gap semiconductor. *Phys. Rev. Lett.* **105**, 136805. https://doi.org/10.1103/PhysRevLett.105.136805 (2010).
16. Splendiani, A. *et al.* Emerging photoluminescence in monolayer MoS_2. *Nano Lett.* **10**, 1271–1275. https://doi.org/10.1021/nl903868w (2010).
17. Wypych, F. & Schöllhorn, R. 1T-MoS_2 a new metallic modification of molybdenum disulfide. *J. Chem. Soc. Chem. Commun.* 19, 1386-1388. https://doi.org/10.1039/C39920001386 (1992).
18. Enyashin, A. N. *et al.* New route for stabilization of 1T-WS_2 and MoS_2 phases. *J. Phys. Chem. C* **115**, 24586–24591. https://doi.org/10.1021/jp2076325 (2011).
19. Sun, X., Wang, Z., Li, Z. & Fu, Y. Q. Origin of structural transformation in mono- and bi-layered molybdenum disulfide. *Sci. Rep.* **6**, 26666. https://doi.org/10.1038/srep26666 (2016).
20. Gao, G. *et al.* Charge mediated semiconducting-to-metallic phase transition in molybdenum disulfide monolayer and hydrogen evolution reaction in new 1T' phase. *J. Phys. Chem. C* **119**, 13124–13128. https://doi.org/10.1021/acs.jpcc.5b04658 (2015).
21. Lin, Y. C., Dumcenco, D. O., Huang, Y. S. & Suenaga, K. Atomic mechanism of the semiconducting-to-metallic phase transition in single-layered MoS_2. *Nat. Nanotechnol.* **9**, 391–396. https://doi.org/10.1038/nnano.2014.64 (2014).
22. Kang, Y. *et al.* Plasmonic hot electron induced structural phase transition in a MoS_2 monolayer. *Adv. Mater.* **26**, 6467–6471. https://doi.org/10.1002/adma.201401802 (2014).
23. Papageorgopoulos, C. A. & Jaegermann, W. Li intercalation across and along the van der Waals surfaces of MoS_2(0001). *Surf. Sci.* **338**, 83–93. https://doi.org/10.1016/0039-6028(95)00544-7 (1995).
24. Föhlisch, A. *et al.* Direct observation of electron dynamics in the attosecond domain. *Nature* **436**, 373–376. https://doi.org/10.1038/nature03833 (2005).
25. Föhlisch, A. *et al.* Verification of the core-hole-clock method using two different time references: attosecond charge transfer in c(4×2)S/Ru(0 0 0 1). *Chem. Phys. Lett.* **434**, 214–217. https://doi.org/10.1016/j.cplett.2006.12.001 (2007).
26. Ceballos, F., Bellus, M. Z., Chiu, H. Y. & Zhao, H. Ultrafast charge separation and indirect exciton formation in a MoS_2-$MoSe_2$ van der Waals heterostructure. *ACS Nano* **8**, 12717–12724. https://doi.org/10.1021/nn505736z (2014).
27. Hong, X. *et al.* Ultrafast charge transfer in atomically thin MoS_2/WS_2 heterostructures. *Nat. Nanotechnol.* **9**, 682–686. https://doi.org/10.1038/nnano.2014.167 (2014).
28. Kühn, D. *et al.* Directional sub-femtosecond charge transfer dynamics and the dimensionality of 1T-TaS_2. *Sci. Rep.* **9**, 488. https://doi.org/10.1038/s41598-018-36637-0 (2019).
29. Garcia-Basabe, Y. *et al.* Species selective charge transfer dynamics in a P3HT/MoS_2 van der Waals heterojunction: fluorescence lifetime microscopy and core hole clock spectroscopy approaches. *Phys. Chem. Chem. Phys.* **21**, 23521–23532. https://doi.org/10.1039/c9cp04431k (2019).
30. Garcia-Basabe, Y. *et al.* Ultrafast charge transfer dynamics pathways in two-dimensional MoS_2-graphene heterostructures: a core-hole clock approach. *Phys. Chem. Chem. Phys.* **19**, 29954–29962. https://doi.org/10.1039/c7cp06283d (2017).

31. Garcia-Basabe, Y. *et al.* Phase transition and electronic structure investigation of MoS_2-reduced graphene oxide nanocomposite decorated with Au nanoparticles. *Nanotechnology* **30**, 475707. https://doi.org/10.1088/1361-6528/ab3c91 (2019).
32. Hanwell, M. D. *et al.* Avogadro: an advanced semantic chemical editor, visualization, and analysis platform. *J. Cheminform.* **4**, 17. https://doi.org/10.1186/1758-2946-4-17 (2012).
33. Eda, G. *et al.* Coherent atomic and electronic heterostructures of single-layer MoS_2. *ACS Nano* **6**, 7311–7317. https://doi.org/10.1021/nn302422x (2012).
34. Jiménez Sandoval, S., Yang, D., Frindt, R. F. & Irwin, J. C. Raman study and lattice dynamics of single molecular layers of MoS_2. *Phys. Rev. B* **44**, 3955–3962. https://doi.org/10.1103/PhysRevB.44.3955 (1991).
35. Eda, G. *et al.* Photoluminescence from chemically exfoliated MoS_2. *Nano Lett.* **11**, 5111–5116. https://doi.org/10.1021/nl201874w (2011).
36. Chaste, J. *et al.* Phase transition in a memristive suspended MoS_2 monolayer probed by opto- and electro- mechanics. *ACS Nano* **14**, 13611–13618. https://doi.org/10.1021/acsnano.0c05721 (2020).
37. Choe, D. H., Sung, H. J. & Chang, K. J. Understanding topological phase transition in monolayer transition metal dichalcogenides. *Phys. Rev. B* **93**, 125109. https://doi.org/10.1103/PhysRevB.93.125109 (2016).
38. Papadopoulos, N., Island, J. O., van der Zant, H. S. J. & Steele, G. A. Investigating laser-induced phase engineering in MoS_2 transistors. *IEEE Trans. Electron. Devices* **65**, 4053–4058, https://doi.org/10.1109/TED.2018.2855215 (2018).
39. Campbell, J. L. & Papp, T. Width of the atomic K-N7 levels. *At. Data Nucl. Data Tables* **77**, 1–56. https://doi.org/10.1006/adnd.2000.0848 (2001).
40. Yu, Y. *et al.* Layer-dependent electrocatalysis of MoS_2 for hydrogen evolution. *Nano Lett.* **14**, 553–558. https://doi.org/10.1021/nl403620g (2014).
41. Sorgenfrei, F. FEMTOSPEX molecules and surfaces: electron spectroscopy setup for time-resolved laser-pump/ X-ray-probe experiments at BESSY II. *J. Large-scale Res. Facilities* **2**, A81. https://doi.org/10.17815/jlsrf-2-87 (2016).
42. Kühn, D. *et al.* Capabilities of angle resolved time of flight electron spectroscopy with the 60° wide angle acceptance lens. *J. Electron Spectrosc. Relat. Phenom.* **224**, 45–50. https://doi.org/10.1016/j.elspec.2017.06.008 (2018).

Acknowledgements

We gratefully acknowledge technical support by the staff of Helmholtz-Zentrum Berlin at BESSY II and Dr. Hikmet Sezen. In particular the experimental support at the "FEMTOSPEX Molecules and Surfaces" endstation at UE56/1 PGM as well as the LowDosePES endstation at the PM4 dipole beamline by E. Giangrisostomi and R. Ovsyannikov for preliminary measurements is acknowledged that made the successful realization of the presented experiment and results possible. A.F. acknowledges funding by FLAG-ERA Graphene Basic Research 2 2017 in project LaMeS DFG project number 400335214 as well as ERC-Advanced Investigator Grant No. 669531 EDAX.

Author contributions

The presented measurements were performed by R.H., N.L.A.N.S., S.N., E.G., D.K, and data handled and analyzed by R.H. The manuscript was written by R.H. and A.F. with significant input from E.G., N.L.A.N.S. and S.N. The research was planned by A.F., R.H., N.L.A.N.S. and directed by A.F. All authors have been given the option to comment the manuscript.

Funding

Open Access funding enabled and organized by Projekt DEAL.

Competing interests

The authors declare no competing interests.

Additional information

Supplementary Information The online version contains supplementary material available at https://doi.org/10.1038/s41598-021-86364-2.

Correspondence and requests for materials should be addressed to R.H.

Reprints and permissions information is available at www.nature.com/reprints.

Publisher's note Springer Nature remains neutral with regard to jurisdictional claims in published maps and institutional affiliations.